

Equilibrium reconstruction in the Madison Symmetric Torus reversed field pinch

J.K. Anderson, C.B. Forest, T.M. Biewer^a, J.S. Sarff and J.C. Wright^b

Department of Physics, University of Wisconsin, Madison, WI 53706, USA

Received 21 December 2002, accepted for publication 18 November 2003

Published 17 December 2003

Online at stacks.iop.org/NF/44/162 (DOI: 10.1088/0029-5515/44/1/018)

Abstract

A non-linear Grad–Shafranov toroidal equilibrium reconstruction code (MSTFit) has been developed for the Madison Symmetric Torus. This is the first such code applied to the unique magnetohydrodynamic (MHD) equilibrium of the reversed field pinch. A new set of toroidal Green's tables have been computed to impose the boundary condition of the close-fitting conducting shell. The non-linear fitting routine is sufficiently versatile for incorporating data from a variety of internal and external diagnostics, including a novel constraint based on orbits from a heavy ion beam probe diagnostic. Utilizing the full complement of internal and external magnetic and pressure diagnostics, MSTFit resolves accurately subtle changes in internal magnetic structure with implications on MHD stability. We show example equilibria that confirm conservation of magnetic helicity during relaxation and two-dimensional equilibrium effects.

PACS numbers: 52.55.Hc

1. Introduction

An accurate determination of the magnetohydrodynamic (MHD) equilibrium (including parallel current density and magnetic field profiles) is of fundamental importance to physics research in the reversed field pinch (RFP). Gradients in the normalized parallel current density ($\lambda = J_{\parallel}/|B|$) profile drive resistive tearing modes, and the associated magnetic fluctuations are responsible for much of the macroscopic dynamics of the RFP [1]. Modification of the λ profile has reduced significantly the magnetic fluctuation levels and increased confinement [2–4], possibly indicating the RFP as an attractive fusion reactor concept. The MHD equilibrium in the RFP has been studied at several levels of sophistication. Taylor's conjecture (global magnetic helicity is conserved as the plasma relaxes to its minimum magnetic energy state [5]) predicts a flat [$\lambda(r) = \text{const}$] profile. This does not agree in detail with the experiment as λ goes to zero at the boundary, but it does predict the monotonic decrease and reversal of the toroidal magnetic field profile. Cylindrical models (constrained by edge magnetic data) that allow the parallel current density to go to zero at the plasma boundary have been used extensively in studies of the RFP equilibrium

[6–8]. However, advanced internal magnetic diagnostics in the Madison Symmetric Torus (MST) RFP show a distinction between the experiment and these one-dimensional models. Two-dimensional studies of the RFP equilibrium have been made (see, e.g. [9]), and this work represents the first detailed studies of experimental equilibria based on experimental data.

Stability calculations are sensitive to subtle changes in the λ profile, and it is thus desirable to determine the MHD equilibrium as accurately as possible, making use of all available data. This has motivated the development of a new code (MSTFit) that is well suited for the unique magnetic structure of the RFP, where poloidal and toroidal magnetic fields are of approximately the same strength and are generated primarily by currents in the plasma and induced currents in the shell. The technique used in the tokamak community [10] has been applied: an axisymmetric solution of Maxwell's equations is found while satisfying radial force balance ($\mathbf{J} \times \mathbf{B} = \nabla P$) and finding the best-fit to all available data. While this is not a new concept, this is the first application of such a code in the RFP. This code differs from previously published equilibrium reconstruction techniques in the treatment of the close-fitting conducting shell and the use of a versatile (but computationally burdensome) non-linear fitting routine. The approach is extensible to many free parameters, and the accuracy of the solution is ultimately limited by the data used to constrain the fit.

^a Current address: Princeton Plasma Physics Laboratory, Princeton, NJ, USA.

^b Current address: PSFC, Massachusetts Institute of Technology, Cambridge, MA, USA.

The MST [11] is a large RFP (1.50 m major radius, 0.52 m minor radius) capable of generating a toroidal plasma current up to 500 kA and a central electron temperature $\lesssim 1000$ eV. A close-fitting, circular cross-section aluminium shell (of 5 cm thickness) surrounds the plasma and acts as the vacuum vessel and single-turn toroidal field winding. The shell has a single poloidal and single toroidal insulating gap through which magnetic flux is inserted.

This paper describes the MSTFit code and provides a handful of illustrative results. Section 2 is a description of the numerical technique used to solve the Grad–Shafranov equation consistently with explicit treatment of the conducting shell. An overview of the diagnostics available and the fitting method are in section 3, along with a specific mention of the method used to constrain the equilibrium based on heavy ion orbits. An example equilibrium that demonstrates the ability of the code to reconstruct accurately internal magnetics and a semi-analytic estimate of the uncertainty in the resulting profiles are presented in section 4. An investigation of helicity conservation during plasma relaxation is revisited [12] using reconstructed profiles. Also presented are the flux surface geometry, which is required for interpretation of temperature and density measurements, and the trapped particle fraction (an inherently two-dimensional phenomenon), which is now readily accessible with a full equilibrium reconstruction.

2. Numerical technique

The Grad–Shafranov equation,

$$\begin{aligned} \Delta^* \psi &= -\mu_0 R J_\phi, \\ J_\phi &= \frac{2\pi F F'}{\mu_0 R} + 2\pi R p', \end{aligned} \quad (1)$$

is a second-order non-linear partial differential equation describing axisymmetric toroidal equilibria. Here, the elliptic operator $\Delta^* = R^2 \nabla \cdot (\nabla / R^2)$, ψ is the poloidal magnetic flux, and the two free functions, $F = R B_\phi = F(\psi)$ (related to the poloidal current flowing between the magnetic axis and a given flux surface) and $p = p(\psi)$ (plasma pressure), are functions of poloidal flux only. The Grad–Shafranov equation derives from the assumption that the magnetic field can be written as $\mathbf{B}(R, Z) = B_\phi(R, Z) \hat{\phi} + \nabla \psi(R, Z) \times \nabla \phi$; and $\mathbf{B} \cdot \nabla \psi = 0$. This is valid for plasmas free of MHD activity—nearly all the time in the tokamak configuration and only during high performance periods in RFP plasmas. In the presence of MHD activity (i.e. $\mathbf{B} = \mathbf{B}_0 + \tilde{\mathbf{b}}$), radial magnetic field perturbations destroy the flux surfaces, $\mathbf{B} \cdot \nabla \psi = \tilde{\mathbf{b}} \cdot \nabla \psi \neq 0$. Under these circumstances and hereafter in this paper, the reconstruction considers only the axisymmetric portion of the magnetic field, and the label ψ is the zeroth-order flux surface label. The poloidal magnetic flux is computed with the appropriate Green’s function and specified toroidal currents in the plasma and shell. MSTFit computes these on an unstructured triangular mesh (shown in figure 1), that divides the 0.85 m² MST cross-section into 746 elements and invokes up–down symmetry; quintic interpolation is used when mapping to higher resolution grids for plotting. The close-fitting shell is modelled as 144 poloidally distributed toroidal current filaments.

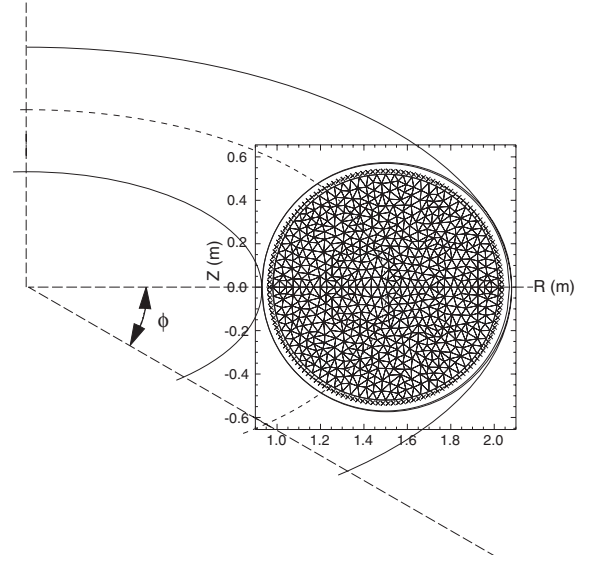


Figure 1. Grid and coordinate system (standard cylindrical) used in equilibrium reconstruction. The triangular mesh grid is up–down symmetric and divides the poloidal cross-section into 746 elements.

Finding a consistent equilibrium is an iterative problem. In practice, the free functions, $F(\psi)$ and $p(\psi)$, are specified and the resulting toroidal current density is computed according to equation (1). The toroidal plasma current and toroidal currents in the vessel are then used to compute the poloidal magnetic flux, which in principle can change the geometry for mapping $F(\psi)$ and $p(\psi)$ to real space. Computations of toroidal current and poloidal flux are repeated until they converge to a consistent equilibrium. A minimization routine then adjusts the profiles of F and P , searching through a large number of equilibria to find the one that best matches the measurements. When the best-fit is found, the code is restarted using the solution as the initial guess to ensure the solution is an absolute (as opposed to a local) extremum.

This technique, illustrated in the flowchart in figure 2, differs somewhat from linear codes in that it finds a consistent equilibrium on each iteration rather than simultaneously solving for the equilibrium and fitting measurements. The advantage is increased versatility, while the cost is computation time. This framework allows the code to forego a standard basis function expansion to describe the free functions, e.g.

$$F'(\psi) = \sum_{i=1}^{M-1} a_i f_i(\psi), \quad (2)$$

where the set of coefficients \mathbf{a} are the free parameters determined by fitting. MSTFit parametrizes the free functions by using spline interpolation through several points. The free parameters are the locations in ψ and functional values of the knots, as sketched in figure 3. Cubic spline interpolation generates very general profiles in this approach, and tension can be added to the splines to further generalize the set of available profiles.

2.1. Green’s function approach

The poloidal flux at any given grid point depends on the toroidal current at all other points, including toroidal currents flowing in

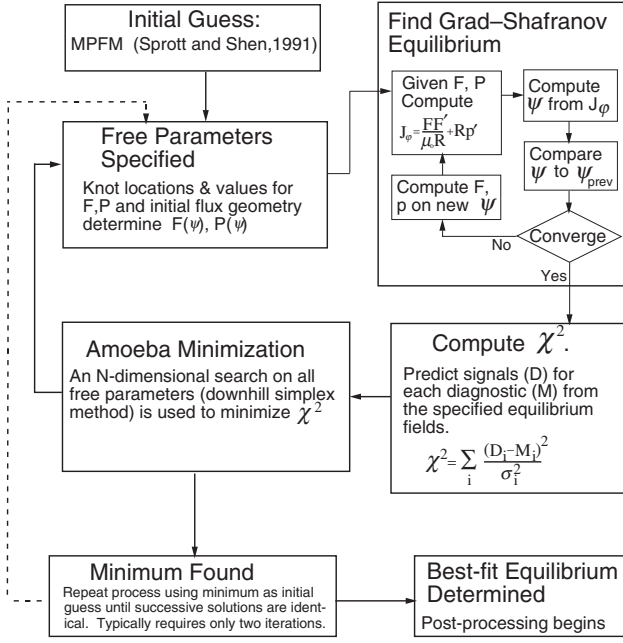


Figure 2. MSTFit flowchart. A consistent Grad–Shafranov equilibrium is found in each iteration before comparing with data. The downhill simplex method is used to minimize χ^2 .

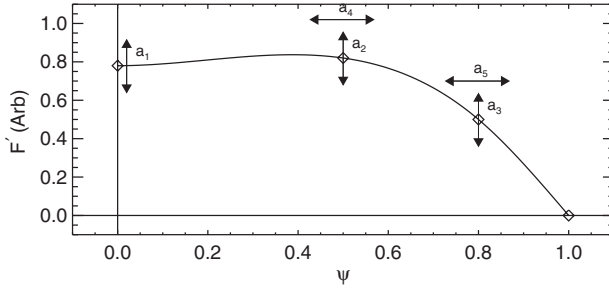


Figure 3. Free parameters used to specify the F' profile. As F' is effectively current density, boundary conditions ensure that the function goes to zero at $\psi = 1$ (no current at boundary) and has a zero derivative at $\psi = 0$ (continuous derivative through the axis).

the shell. The general toroidal Green’s function (G) computes the poloidal flux at the point (R, Z) due to a unit toroidal current at (R', Z') :

$$\psi_{\text{pol}}(R, Z) = \int \int_{A'} G(R', Z'; R, Z) J_{\phi}(R', Z') dA', \quad (3)$$

where

$$\frac{-R}{2\pi\mu_0} \nabla \cdot \left(\frac{\nabla G}{R^2} \right) = \delta(R - R') \delta(Z - Z'). \quad (4)$$

In a vacuum (no conducting shell), the appropriate Green’s function is [13]

$$G = \frac{\mu_0}{\pi k} \sqrt{\frac{R'}{R}} \left(\left(1 - \frac{1}{2}k^2 \right) K(k) - E(k) \right), \quad (5)$$

where $E(k)$ and $K(k)$ are elliptic integrals of the first kind and $k^2 = 4RR' / ((R + R')^2 + Z^2)$.

Integration of equation (3) is replaced by summation on the discrete grid, which reduces to matrix multiplication as

$$\psi_{\text{pol}} = \mathbf{G} \cdot \mathbf{I}_{\phi}, \quad (6)$$

where the matrix \mathbf{G} computes the flux at every point due to all currents (\mathbf{I}_{ϕ}) on the grid. Similarly, the spatial derivatives of $G(R', Z'; R, Z)$ relate the components of the poloidal magnetic field (B_R and B_Z) to \mathbf{I}_{ϕ} .

The close-fitting conducting shell imposes a boundary condition of constant flux at its surface, and currents flowing in the shell must be included when computing poloidal flux. A Green’s function that satisfies the boundary condition (while implicitly finding the necessary shell currents) has been constructed. Equation (6) is modified to include contributions from currents in the vessel, or

$$\psi_{\text{pol}} = \mathbf{G}_p \cdot \mathbf{I}_{\phi} + \mathbf{G}_v \cdot \mathbf{I}_{\text{ves}}, \quad (7)$$

where \mathbf{G}_p is the plasma table and \mathbf{G}_v computes flux on the plasma grid due to currents in the vessel.

The boundary flux is set to zero to enforce the boundary condition, summarized by the matrix equation

$$\bar{\mathbf{0}} = \mathbf{G}_{\text{ap}} \times \bar{\mathbf{I}} + \mathbf{G}_{\text{av}} \times \bar{\mathbf{I}}_{\text{ves0}}, \quad (8)$$

where \mathbf{G}_{ap} and \mathbf{G}_{av} are the matrices that compute flux at the vessel surface due to currents in the plasma and vessel, respectively. Here, $\bar{\mathbf{I}}_{\text{ves0}}$ is the matrix where each column is the set of vessel currents that set the boundary flux to zero for a particular unit current within the plasma. In practice, the currents are computed as individual vectors. \mathbf{G}_{ap} is dotted with the i th unit vector to determine the vector of vessel currents (the i th column of $\bar{\mathbf{I}}_{\text{ves0}}$) for the i th filament within the plasma. Each column operation is a set of over-specified linear equations, and singular value decomposition is used to determine the vessel currents. The fixed-boundary Green’s table is

$$\mathbf{G}_{\text{fixed}} = \mathbf{G}_p + \mathbf{G}_v \times \bar{\mathbf{I}}_{\text{ves0}} \quad (9)$$

and the flux within the plasma is computed by $\psi_{\text{pol}} = \mathbf{G}_{\text{fixed}} \cdot \mathbf{I}_{\phi}$.

The correction to the Green’s functions due to the vessel current is demonstrated in figure 4, where the flux is computed for unit currents in two example locations. Figure 4(a) is the flux computed for a unit current (along with the up–down symmetric complementary current) off the midplane using the free-boundary table. Figure 4(b) is the free-boundary flux computed for a current located near the conducting wall on the midplane. Clearly, multiple flux surfaces intersect the shell. Figures 4(c) and (d) show the flux contours for the same currents using the fixed-boundary Green’s table, and the outer flux surfaces conform to the shell; the boundary flux is constant to within floating point accuracy in reconstructed equilibria. The vessel currents can be viewed for a reconstructed equilibrium (example in figure 6), and it is noted that the distribution is consistent with the single turn resistance of the shell: minimum current at maximum major radius.

3. Data fitting

The code searches through a large number of equilibria in an attempt to find the best-fit to all available data. The method of evaluation is computing a cost function, χ^2 :

$$\chi^2 \equiv \sum_i \frac{(D_i - M_i)^2}{\sigma_i^2}, \quad (10)$$

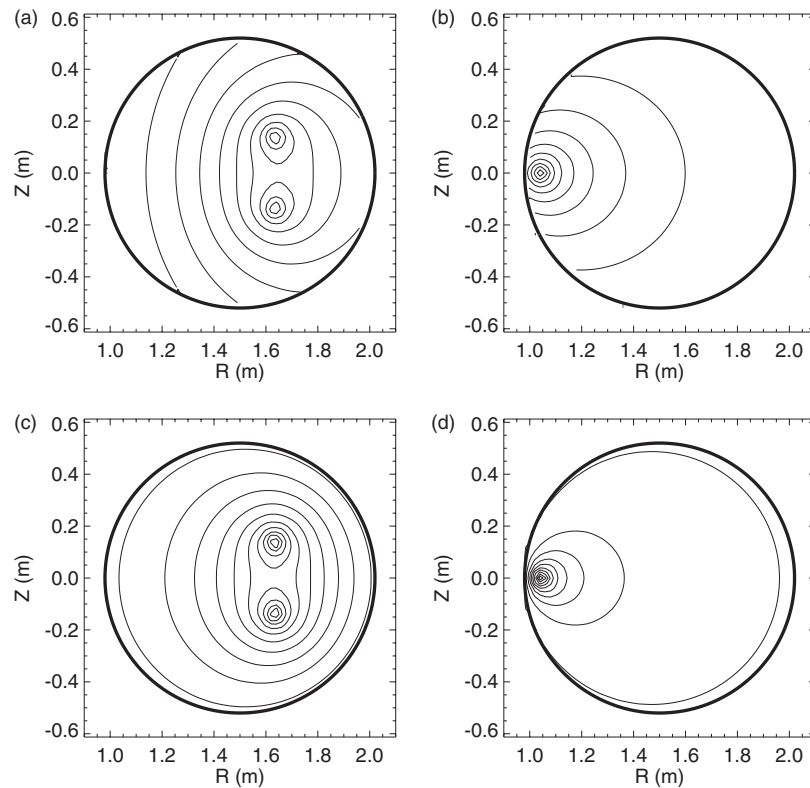


Figure 4. Flux due to a unit current calculated using free- and fixed-boundary Green’s tables. Plots (a) and (b) use the free-boundary tables for computing the flux due to unit currents; multiple flux contours intersect the conducting shell. Plots (c) and (d) are the flux computed for the same two current filaments using the fixed-boundary tables, and the flux contours conform to the vessel. Note up–down symmetry is enforced in these calculations.

where each datum, D_i , is specified with an experimental uncertainty σ_i . From the equilibrium profiles, a predicted signal, M_i , is made for each measurement. The exact method for computing the predicted signal is different for each diagnostic and varies considerably in complexity.

3.1. Pressure diagnostics

The pressure profile in MST is measured using several diagnostics for electron and ion contributions. A Thomson scattering temperature diagnostic and a multi-chord far-infrared (FIR) interferometer measure the electron dynamics. Information on the ion pressure is ascertained from several diagnostics, including a Rutherford scattering system [14] (bulk ion temperature and density), and charge-exchange recombination spectroscopy [15] and ion dynamics spectroscopy [16] systems (impurity temperature), and NIR bremsstrahlung measurement gives some information on impurity concentrations. These data are used to determine the best-fit pressure profile by independently fitting profiles to the electron temperature and density and adding estimates of the ion contributions. The pressure gradient term in the Grad–Shafranov equation is generated by taking the spatial derivative in flux geometry. This term is typically smaller than the FF' term but not negligible.

3.2. External magnetic diagnostics

Several edge diagnostics are a necessary part of the equilibrium reconstruction. Measurements of the total plasma current,

total toroidal magnetic flux, boundary toroidal magnetic field, and poloidal asymmetry factor are made with non-intrusive diagnostics at the plasma boundary. Under some plasma conditions, the edge ($r/a > 0.8$) of the plasma can be probed to measure current density or magnetic field levels directly. These data are incorporated into the equilibrium reconstruction when available.

3.3. Internal magnetic diagnostics

Information solely from edge diagnostics cannot determine the internal structure of the equilibrium profiles accurately [17], and therefore the internal magnetic diagnostics are crucial to the equilibrium reconstruction. A multi-chord Faraday rotation polarimeter [18] measures line integrals of the vertical component of the poloidal field and electron density and constrains the toroidal current density. A direct measurement of the magnitude of the near-axis magnetic field with a motional Stark effect diagnostic [15] provides a very strong constraint to the equilibrium. These diagnostics have been used in previous equilibrium reconstruction work [10], although fitting $|B|$ is considerably less complicated in this non-linear routine as profiles of each component of the magnetic field are determined in each iteration.

A novel constraint to the equilibrium reconstruction also allowed with this fitting routine is provided by a heavy ion beam probe (HIBP) [19] in MST. A primary beam of ions (Na^+ , K^+ , Cs^+ , or others) is sent into the plasma at a specified velocity (speed and direction). The ions travel across the plasma

according to the Lorentz force, which is dominated by the $v \times B$ term for the high energy ($\sim 40\text{--}80$ keV) ions. A fraction of the ions in the beam undergo a second ionization, producing a fan of secondary (doubly charged) ions that follow different trajectories. Secondary ions from a localized volume within the plasma exit through a port separated from the injection port in R , Z , and ϕ and are measured. Constraint of the equilibrium is provided by tracing the orbit of the primary ions (and the reverse of the secondary orbit) from the entrance (exit) port into the machine. In an experiment where the signal is observed, the two trajectories must intersect and be nearly tangential at some point in the plasma. Constraining the equilibrium reconstruction is done by simply adding a term to the χ^2 , following equation (10), given by

$$\chi_{\text{HIBP}}^2 = \left(\frac{\Delta D}{0.005} \right)^2 + \left(\frac{\Delta v}{0.05} \right)^2, \quad (11)$$

where ΔD is the closest approach between the primary and secondary orbits and Δv is the difference in the velocity unit vector (direction only) at the point of intersection. The denominator values of 0.005 m and 0.05 (dimensionless) are nominal uncertainties, corresponding to the typical beam width within the plasma. Computation of the orbits' closest approach

and tangency is trivial with the fully specified magnetic field profile at each iteration.

A comparison between the reconstructed equilibrium and the internal diagnostic data used to constrain the fit is shown in figure 5; this particular reconstruction is detailed in section 4. Figure 5(a) shows the agreement between the measured $|B|$ over a finite region near the plasma core, and figure 5(b) is the fit to Thomson scattering electron temperature measurements, which determines the pressure profile in conjunction with the electron density profile. The upper plot in figure 5(c) contains the Faraday rotation data (six of 11 chords were online during this experiment), and the lower plot is the line-integrated density on all 11 chords with the reconstructed profile. Figure 5(d) demonstrates the intersection of the primary (dotted) and secondary (dashed) beam orbits which constrains the reconstructed magnetic field profiles. The top plot is an (R, Z) cross-section of the MST, and the lower is a top view of the torus showing the toroidal deflection of the beams. This reconstruction also matches edge measurements (plasma current, total toroidal flux, and toroidal field at the wall) to within 1%. The equilibrium is further constrained by a poloidally resolved measurement of B_θ via an array of Mirnov coils.

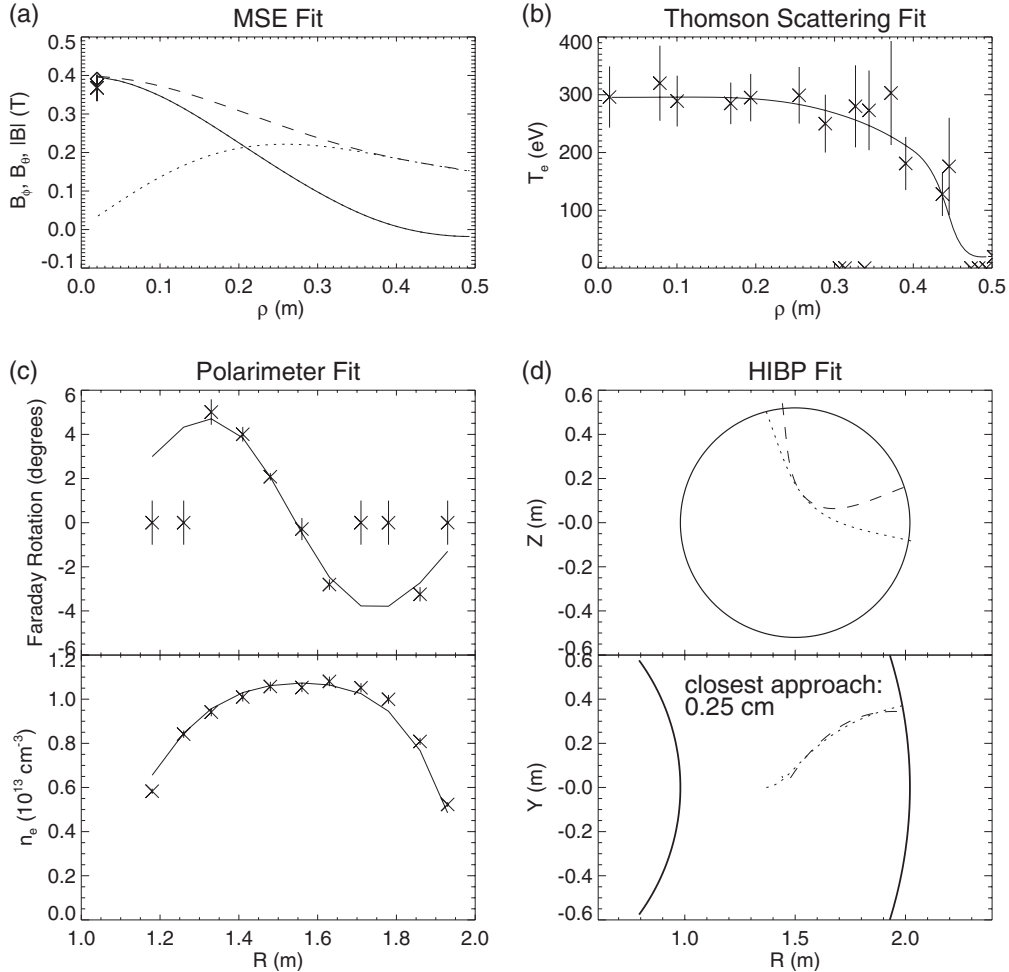


Figure 5. Fit to data in a typical equilibrium reconstruction; (a) through (c) show the agreement among the MSE, Thomson scattering, and FIR polarimeter: data are shown with error bars, and the fits are the solid lines. Panel (d) is the fit of the HIBP data: the cross sectional and top views show that the orbits from the injection port and from the exit port meet in the plasma interior.

The accuracy and the generality of the code have been tested using ideal data. Several current density profiles, ranging from extremely peaked to extremely flat, were manually generated and used in conjunction with a typical pressure profile to predict the signals from each of the main diagnostics. The generated profiles were not created with the basis functions described in figure 3 to ensure iteration of the free parameters during reconstruction. The ideal data were then used as inputs to the code, and this yielded positive results. The free parameters and basis functions were versatile enough to reconstruct all current density profiles tested, including those that go beyond the range of experimentally observed profiles. The fitting accuracy was also very good, with the signals predicted by the reconstructed equilibria matching the ideal data (better than 0.5% accuracy) and matching the mock current density profile to better than 2% at all radii. It is expected that this accuracy could be improved with more diagnostic coverage of the plasma.

Further studies aimed at testing the code's ability to reconstruct internal structure were undertaken by creating significantly different current density profiles with identical edge values of plasma current, toroidal flux, and boundary toroidal field. Signals expected from the internal diagnostics were again computed, and the reconstruction reproduced the current density profile to similar accuracy. The stability of the code was tested using mock data that were purposely inconsistent between two diagnostics. The result was as expected: the reconstructed equilibrium minimized the cost function (χ^2), and uncertainty in the reconstructed equilibria (see section 4.1) was considerably higher.

4. Reconstructed equilibria

Figures 6 and 7 are the results of an equilibrium reconstruction of a standard, low temperature 380 kA MST discharge based on multiple internal diagnostics (data and reconstruction are shown in figure 5). Details on the experiment for which these particular plasmas were produced can be found in [20]. The surfaces of poloidal flux (figures 6(a) and (b)) are nearly circular, with a magnetic axis (figure 6(c)) shifted approximately 0.05 m from the geometric centre. Again, we note that the poloidal flux calculated here is from the axisymmetric portion of the magnetic field; in the presence of magnetic fluctuations, the nested toroidal flux surfaces can be destroyed. The effective one-dimensional minor radius coordinate (ρ) is defined by flux surface volume (figure 6(d)), and the toroidal current induced in the vessel is shown (figure 6(e)). A subset of the flux surface averaged quantities that characterize the equilibrium are plotted versus ρ in figure 7. Shown are the free functions, F (figure 7(a)) and P (figure 7(b)), along with the profiles that generate toroidal current in the Grad-Shafranov equation, FF' (figure 7(c)) and P' (figure 7(d)); quantities computed after the free functions are determined include: the parallel current density (solid) and toroidal current density (dashed) in figure 7(e); the total (solid), toroidal (dashed), and poloidal (dotted) magnetic field in figure 7(f); the safety factor (figure 7(g)), normalized parallel current density, λ (figure 7(h)), and magnetic energy stored from zero to radius ρ (figure 7(i)); and finally the magnetic helicity $K = \int \phi d\psi + \int \psi d\phi$ from zero to radius ρ

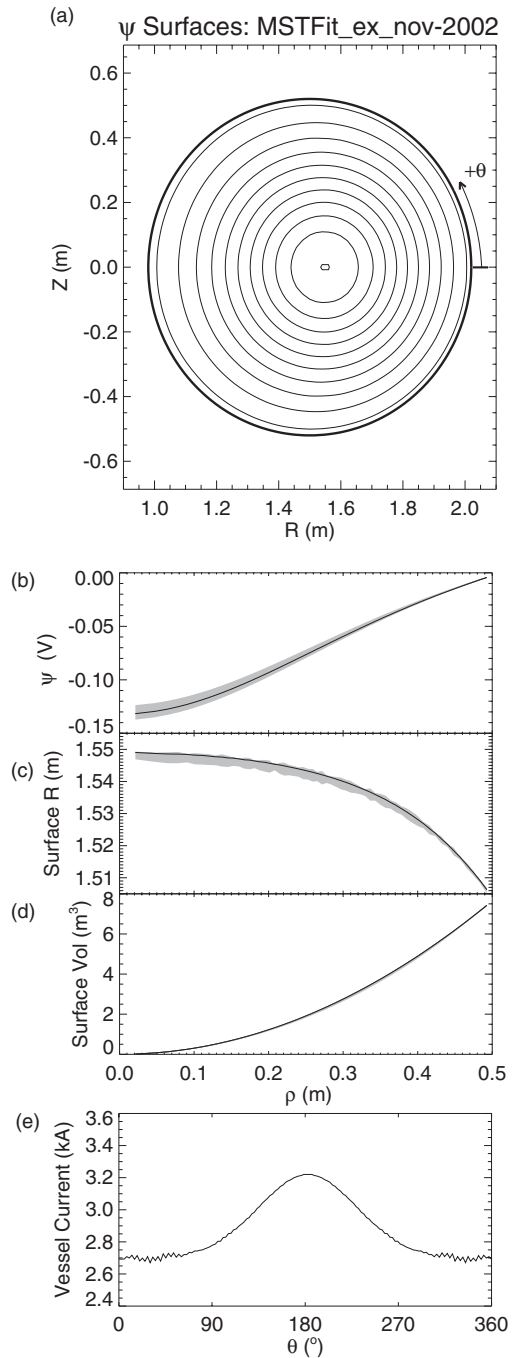


Figure 6. Flux surface geometry for a typical equilibrium reconstruction. The poloidal flux (b) ranges from 0 at the boundary to about -0.13 V s in the core; the surfaces of constant flux (a) are nearly circular with central radii (c) and volumes (d) shown. Plot (e) is the distribution of toroidal current induced in the vessel.

in figure 7(j). Several other profiles and zero-dimensional quantities are also computed but not shown here in the interest of brevity.

4.1. Equilibrium uncertainty analysis

A complete uncertainty analysis must be performed in order to determine confidence levels in the equilibrium quantities. In principle, a Monte Carlo analysis can be performed on

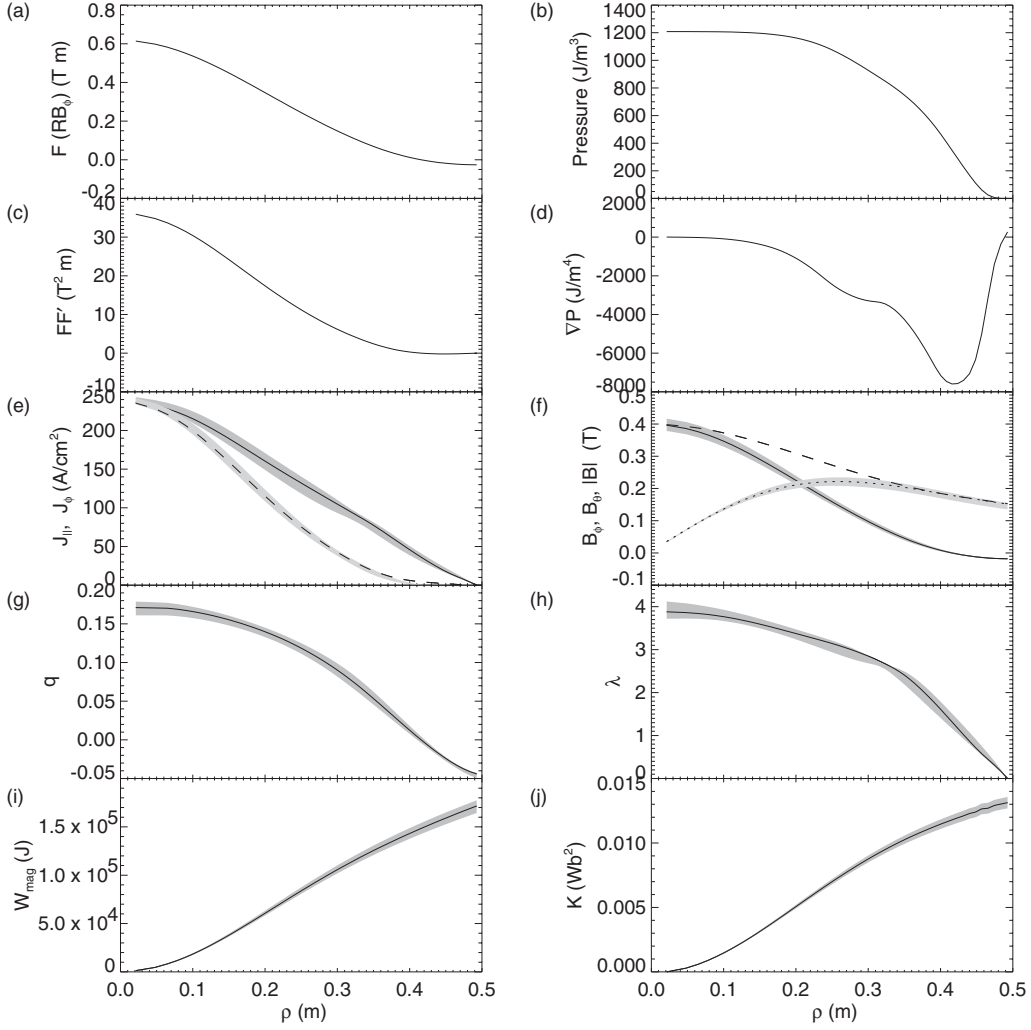


Figure 7. Reconstructed magnetic profiles. The free functions, F (a) and pressure (b), are shown along with their contributions to toroidal current density, FF' (c), and ∇P (d). The resulting current density (parallel solid line, toroidal dotted line in (e)) is plotted. The total (—), toroidal (- - -), and poloidal (· · · · ·) magnetic field profiles are computed (f). The safety factor profile (q , (g)) and normalized parallel current density, ($\lambda = \mu_0 a J_{||} / |B|$) (h) are plotted, along with the magnetic energy (i) and magnetic helicity (j) enclosed by radius ρ .

the equilibrium calculation: data such as the plasma current, edge magnetic field measurements, polarimetry signals, etc can be varied within their uncertainty, and the equilibrium fitting can be computed for many sets of the varied data. This is computationally burdensome and is prohibitively slow.

MSTFit uses instead a semi-analytic approach to estimate the uncertainty in the equilibrium free parameters. The minimized quantity, χ^2 , is a function of N variables (the free parameters of the fit denoted by \mathbf{a}_i), and can be Taylor expanded about the minimum (keeping terms to second-order and noting that the first derivatives must vanish at the minimum):

$$\chi^2 = \chi_0^2 + \frac{1}{2} \sum_{i,j=1}^N \frac{\partial^2 \chi_0^2}{\partial a_i \partial a_j} \delta a_i \delta a_j, \quad (12)$$

where the subscript 0 denotes evaluation of the function at its minimum and δa_i is the deviation of the i th free parameter from its value at the minimum.

The distance a given free parameter must vary from the minimum to increase the χ^2 a specified amount is proportional to the standard deviation in that parameter's value. It is shown

in [21,22] that varying a parameter a_i by one standard deviation leads to a reduced χ^2 increase of 1. In the vicinity of the minimum,

$$\chi^2 = \frac{\delta a_i^2}{\sigma_i^2} + C \quad (13)$$

defines the uncertainty in a free parameter (σ_i) and holds where C is a function of all other a_j .

Each free parameter is varied independently to compute the second derivative near the minimum, and the uncertainty in a given free parameter is

$$\sigma_j^2 = 2 \left(\frac{\partial^2 \chi^2}{\partial a_j^2} \right)^{-1}. \quad (14)$$

Figure 8 is a plot of the χ^2 space versus two of the free parameters and shows the quadratic nature in each free parameter.

Finally, the set of free parameters are varied within their calculated uncertainties (several iterations) and the equilibrium quantities are computed each time. The resulting envelope

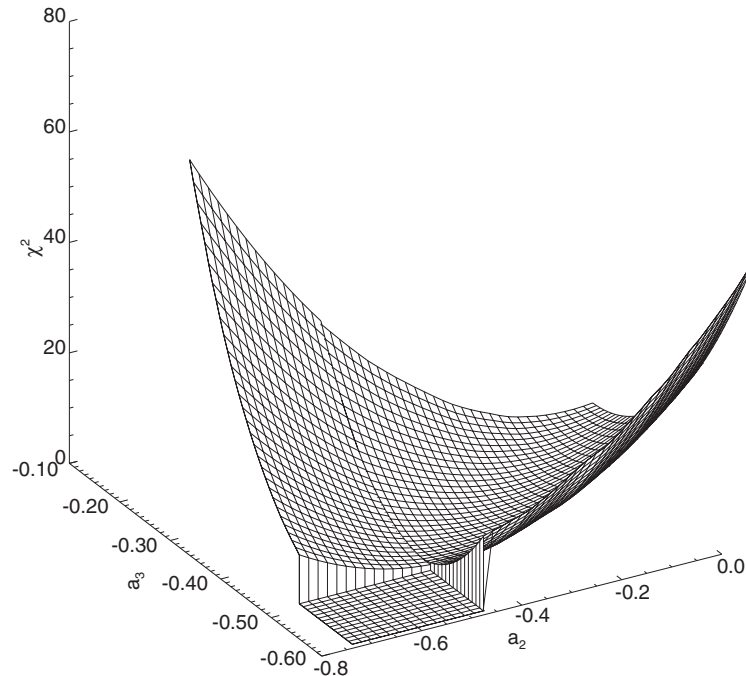


Figure 8. Surface plot of χ^2 . The x - and y -axes are two free parameters varied about their minimum. The quadratic nature of the surface near the minimum is illustrated by excluding the front left quadrant from the plot.

on output profiles is the experimental uncertainty in that quantity; results of this analysis are shown in figures 6 and 7 as shaded regions about the equilibrium profile. Note that the relative uncertainty is highest in the core for edge-constrained profiles such as poloidal flux (figure 6(a)), current density (figure 7(e)), toroidal magnetic field (figure 7(f)), and safety factor (figure 7(g)) and ranges from 6% to 8% for this reconstruction. The uncertainty is largest at the edge for integral quantities such as total magnetic stored energy (figure 7(i)) and helicity (figure 7(j)); and we note that these integral quantities have a lower maximum uncertainty (3–5%) than the edge-constrained profiles.

4.2. RFP equilibrium studies

A full two-dimensional equilibrium reconstruction is an important tool for RFP research. MSTFit runs several post-processing routines after the equilibrium is determined. Packages include a particle transport, an energy transport, and a one-dimensional stability analysis, and the flux geometry is crucial for interpretation of line-integrated emission measurements. We present here two useful examples of studies accessible with MSTFit.

The conservation of magnetic helicity during plasma relaxation is re-examined following Ji *et al* [12], with improved measurements of the magnetic field profiles. The RFP equilibrium relaxes periodically to a minimum energy state referred to as the sawtooth cycle [23]. From an initially minimum energy state (flat λ profile), the profiles of current density and λ gradually become peaked as more current is driven in the hotter, less resistive core of the plasma. At a critical point, current-driven modes become unstable and the MHD dynamo redistributes the current and generates toroidal flux rapidly. The current density and toroidal magnetic field

profiles are both flattened, and a decrease in magnetic energy is measured. Ji found a 4.0–10.5% decrease in magnetic energy during relaxation (depending on the model used), and the same models showed only a 1.3–5.1% decrease in helicity, modestly supporting Taylor’s relaxation theory that global helicity is conserved. Figure 9 summarizes the same analysis using MSTFit on a set of 380 kA plasmas. The magnetic energy is shown to decrease (zero-suppressed plot in figure 9(a)) by approximately 8% at the crash (well outside the error bars), while the magnetic helicity decreases only about 1% (figure 9(b)), with a larger experimental uncertainty. Also shown in figure 9 are the radial profiles of the magnetic energy density (figure 9(c)) and helicity density (figure 9(d)) versus minor radius before (solid line) and after (dashed line) the sawtooth crash. These plots illustrate the drop in magnetic energy at the crash and the radial transport (but global conservation) of helicity.

A second exercise carried out with MSTFit is a calculation of the trapped particle fraction [24] as

$$f_t = 1 - \frac{3}{4} \langle B^2 \rangle \int_0^{\lambda_c} \frac{\lambda d\lambda}{\sqrt{1 - \lambda B}}, \quad (15)$$

where $\lambda = \mu/E$ is the pitch angle, defined by the ratio of magnetic moment to total kinetic energy. The critical value occurs when the pitch angle lies on the boundary of the loss cone, $\lambda_c = 1/B_{\max}$; particles circulate for $0 \leq \lambda \leq \lambda_c$ and are trapped for $\lambda_c \leq \lambda \leq 1/B_{\min}$. The RFP does not have a tokamak-like high field side as the maximum $|B|$ is near the magnetic axis; however, there is significant variation in field strength along a flux surface. Figure 10(a) shows the $|B|$ variation along the surface that defines $\rho = 0.21$ m; the non-zero variation demonstrates the two-dimensional nature of the RFP equilibrium. Figure 10(b) is a plot of trapped fraction

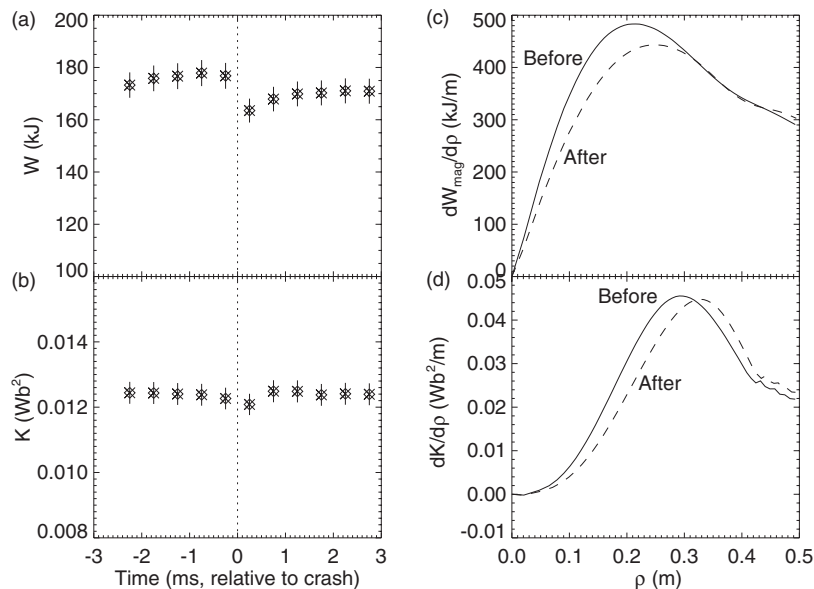


Figure 9. Helicity conservation during a relaxation event. Panels (a) and (b) are the total magnetic energy and helicity versus time relative to the sawtooth crash. Panels (c) and (d) show the profiles of magnetic energy and helicity density before and after relaxation.

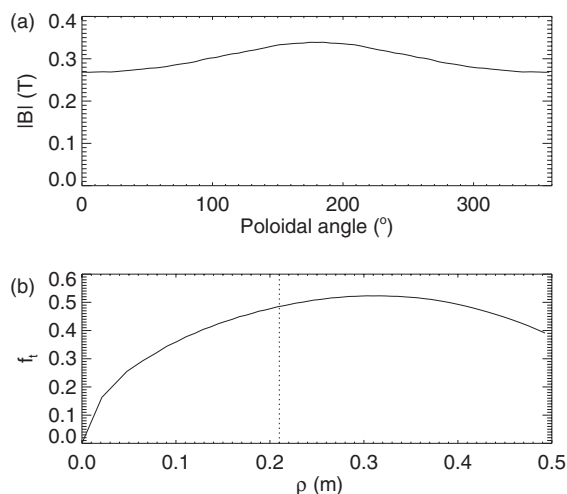


Figure 10. Two-dimensional equilibrium effects. Plot (a) is the variation of $|B|$ along the flux surface whose volume defines $\rho = 0.21$ m; plot (b) is the trapped fraction versus minor radius from a 380 kA standard MST plasma.

versus minor radius. The peak value of 50% agrees with estimates based on assumed, physically reasonable current density profiles in two-dimensional RFP equilibrium studies and implies there is a significant neoclassical correction to the resistivity profile [9].

5. Summary

MSTFit is a new toroidal equilibrium reconstruction code developed for the RFP with the ability to incorporate data from all diagnostics due to its versatile numerical technique. The free-boundary toroidal current loop Green's tables have been modified to impose the constraint of a close-fitting conducting shell, and a full non-linear search of parameter space finds the best-fit to the data. The set of post-processing routines is useful

for inversion of line-integrated data and facilitates particle and energy transport and MHD stability analyses. We have presented two exercises using reconstructed equilibria: the first strengthens previous work demonstrating the conservation of magnetic helicity during plasma relaxation in the MST and the second demonstrates the two-dimensional nature of the RFP equilibrium, implying neoclassical effects cannot be neglected in studies of plasma resistivity.

Acknowledgments

The authors are indebted to the entire MST group and collaborators for access to data from all diagnostics. This work is supported by the US Department of Energy and the Oak Ridge Institute for Science and Education Magnetic Fusion Science Fellowship programme.

References

- [1] Prager S.C. 1999 *Plasma Phys. Control. Fusion* **41** A129
- [2] Sarff J.S., Hokin S.A., Ji H., Prager S.C. and Sovinec C.R. 1994 *Phys. Rev. Lett.* **72** 3670
- [3] Bartiromo R. *et al* 1999 *Phys. Plasmas* **6** 1830
- [4] Chapman B.E. *et al* 2001 *Phys. Rev. Lett.* **87** 205001
- [5] Taylor J.B. 1974 *Phys. Rev. Lett.* **33** 1139
- [6] Schoenberg K.F., Gribble R.F. and Phillips J.A. 1982 *Nucl. Fusion* **22** 1433
- [7] Shen W. and Sprott J.C. 1991 *Phys. Fluids B* **3** 1225
- [8] Antoni V., Martin P. and Ortolani S. 1989 *Nucl. Fusion* **29** 1759
- [9] Stoneking M.R., Chapman J.T., Den Hartog D.J., Fiksel G., Prager S.C. and Sarff J.S. 1998 *Phys. Plasmas* **5** 1004
- [10] Lao L.L., Ferron J.R., Groebner R.J., Howl W., John H.S., Strait E.J. and Taylor T.S. 1990 *Nucl. Fusion* **30** 1035
- [11] Dexter R.N., Kerst D.W., Lovell T.W., Prager S.C. and Sprott J.C. 1991 *Fusion Technol.* **19** 131
- [12] Ji H., Prager S.C. and Sarff J.S. 1995 *Phys. Rev. Lett.* **74** 2945
- [13] Jackson J.D. 1975 *Classical Electrodynamics* (New York: Wiley)
- [14] Reardon J.C. *et al* 2001 *Rev. Sci. Instrum.* **72** 598

-
- [15] Craig D., Den Hartog D.J., Fiksel G., Davydenko V.I. and Ivanov A.A. 2001 *Rev. Sci. Instrum.* **72** 1008
- [16] Den Hartog D.J., Chapman J.T., Craig D., Fiksel G., Fontana P.W., Prager S.C. and Sarff J.S. 1999 *Phys. Plasmas* **6** 1813
- [17] Pustovitov V.D. 2001 *Nucl. Fusion* **41** 721
- [18] Brower D.L. *et al* 2001 *Rev. Sci. Instrum.* **72** 1077
- [19] Lei J., Shah U., Demers D.R., Connor K.A. and Schoch P.M. 2001 *Rev. Sci. Instrum.* **72** 564
- [20] Anderson J.K. 2001 *PhD Thesis* University of Wisconsin-Madison
- [21] Bevington P.R. and Robinson D.K. 1992 *Data Reduction and Error Analysis for the Physical Sciences* (New York: McGraw-Hill)
- [22] Arndt R.A. and MacGregor M.H. 1966 *Methods Comput. Phys.* **6** 253
- [23] Hokin S. *et al* 1991 *Phys. Fluids B* **3** 2241
- [24] Hirshman S.P. and Sigmar D.J. 1981 *Nucl. Fusion* **21** 1079